

RESEARCH ARTICLE

10.1002/2015JB012374

This article is a companion to Liu *et al.* [2015] doi:10.1002/2015JB012372.

Key Points:

- Yielding failure of element is considered in the discrete element method
- Failure angle increases with the increasing aspect ratio of yielding ellipse
- Pattern of wiggly CBs is related to the yielding stress and cement strength

Correspondence to:

C. Liu,
chunliu@nju.edu.cn

Citation:

Liu, C., D. D. Pollard, K. Gu, and B. Shi (2016), Mechanism of formation of wiggly compaction bands in porous sandstone: 2. Numerical simulation using discrete element method, *J. Geophys. Res. Solid Earth*, 120, 8153–8168, doi:10.1002/2015JB012374.

Received 20 JUL 2015

Accepted 13 NOV 2015

Accepted article online 17 NOV 2015

Published online 15 DEC 2015

Mechanism of formation of wiggly compaction bands in porous sandstone: 2. Numerical simulation using discrete element method

Chun Liu^{1,2,3}, David D. Pollard², Kai Gu^{1,3}, and Bin Shi¹

¹School of Earth Sciences and Engineering, Nanjing University, Nanjing, China, ²Department of Geological and Environmental Sciences, Stanford University, Stanford, California, USA, ³Suzhou High-Tech Institute, Nanjing University, Suzhou, China

Abstract Wiggly compaction bands in porous aeolian sandstone vary from chevron shape to wavy shape to nearly straight. In some outcrops these variations occur along a single band. A bonded close-packed discrete element model is used to investigate what mechanical properties control the formation of wiggly compaction bands (CBs). To simulate the volumetric yielding failure of porous sandstone, a discrete element shrinks when the force state of one of its bonds reaches the yielding cap defined by the failure force and the aspect ratio (k) of the yielding ellipse. A Matlab code “MatDEM^{3D}” has been developed on the basis of this enhanced discrete element method. Mechanical parameters of elements are chosen according to the elastic properties and the strengths of porous sandstone. In numerical simulations, the failure angle between the band segment and maximum principle stress decreases from 90° to approximately 45° as k increases from 0.5 to 2, and compaction bands vary from straight to chevron shape. With increasing strain, subsequent compaction occurs inside or beside compacted elements, which leads to further compaction and thickening of bands. The simulations indicate that a greater yielding stress promotes chevron CBs, and a greater cement strength promotes straight CBs. Combined with the microscopic analysis introduced in the companion paper, we conclude that the shape of wiggly CBs is controlled by the mechanical properties of sandstone, including the aspect ratio of the yielding ellipse, the critical yielding stress, and the cement strength, which are determined primarily by petrophysical attributes, e.g., grain sorting, porosity, and cementation.

1. Introduction

Compaction bands (CBs) are tabular structures formed in porous granular sedimentary rock (e.g., sandstone) and result from strain localization to narrow tabular bands. They represent one kinematic end-member of the family of deformation bands [Aydin *et al.*, 2006]. At the microscale, the formation of CBs involves fracturing, grain rotation, and pore collapse [Mollema and Antonellini, 1996; Sternlof *et al.*, 2005; Eichhubl *et al.*, 2010]. Fluid transport (e.g., of ground water and hydrocarbon resources) and the stress field may be significantly changed as CBs form, due to the loss of porosity and compaction [Sternlof *et al.*, 2004; Deng *et al.*, 2015a]. Compaction bands were observed first in the Valley of Fire State Park, Nevada [Hill, 1989], and later in the Kaibab monocline, Utah [Mollema and Antonellini, 1996].

Hill [1989] identified two types of tabular CBs (T1 and T2) that form a conjugate set with a dihedral angle of approximately 90° (Figure 1b) and wiggly CBs (T3) with a zigzag trace (Figures 1a and 1b). As shown in Figure 1a, the wiggly CBs have alternating segments subparallel to T1 and T2, and show chevron (T3₁) or wavy (T3₂) patterns. They became nearly straight CBs (T3₃), when the angle between the neighboring segments increase to approximately 180°. Via force chain analysis of thin sections, Eichhubl *et al.* [2010] inferred that the wiggly CBs were perpendicular to the direction of maximum principle stress (σ_1 , azimuth is approximately 104°), and the tabular T1 and T2 CBs are shear-enhanced CBs that form at 38 to 53° to σ_1 . Therefore, in Figure 1a, the failure angle between the wiggly band segments and the direction of σ_1 increases from chevron (approximately 45°) to wavy (65°) to straight (90°), and only the straight T3₃ CBs result from pure compaction. Compaction bands with irregular zigzag shape also have been produced in laboratory triaxial compressive tests of porous sandstone [e.g., Wong *et al.*, 2001; Baud *et al.*, 2004]. However, uncertainties about the mechanism of formation of wiggly CBs raise the question: what petrophysical attributes and mechanical properties control the formation of CBs with these different shapes?

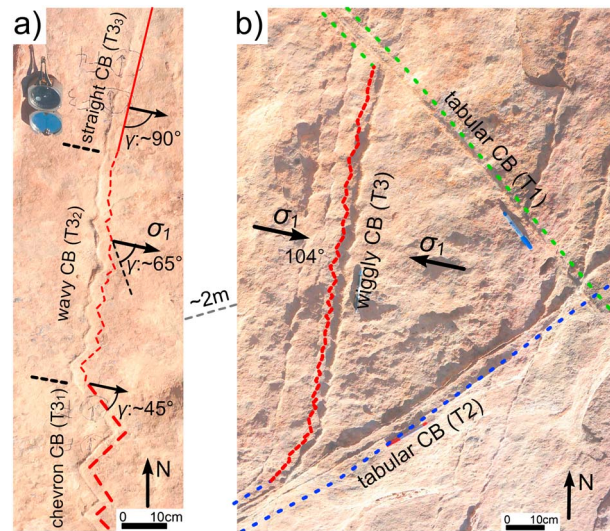


Figure 1. Outcrop photographs taken in the area studied by Hill [1989]. The azimuth of the estimated maximum compressive stress (σ_1) is approximately 104° . (a) Transition of band type from chevron to wavy to straight CBs, as failure angle (γ) increases from approximately 45° to 65° to 90° . (b) Wiggly CBs merged into tabular shear-enhanced CBs. Figure 1b was taken about 2 m from Figure 1a.

The host rock of compaction bands has high porosity [Sternlof *et al.*, 2005; Liu *et al.*, 2015], and the loss of porosity is a primary characteristic of CBs [Sternlof *et al.*, 2005]. For a rock that exhibits a significant component of compactive yielding during deformation, such as the porous sandstone, there is a cap on graphs, for example, of deviatoric stress versus effective mean stress, that defines inelastic volume strain yielding [Olsson, 1999; Issen and Rudnicki, 2000; Issen and Rudnicki, 2001]. The yielding envelope tends to shrink with increasing porosity and may also be influenced by grain size, cementation, and clay content [Wong and Baud, 2012]. Previous studies have shown that the cap model of the yield condition is appropriate for porous sandstones [e.g., Wong *et al.*, 1997; Rudnicki, 2004].

A series of theoretical analyses [e.g., Aydin *et al.*, 2006; Chemenda, 2009; Das *et al.*, 2011] have been proposed to interpret the mechanics of formation of compaction bands. Numerical models also have been used to investigate the generation and the propagation of CBs, including a spring network model [Katsman *et al.*, 2005], finite difference model [e.g., Chemenda, 2009; Chemenda, 2011; Chemenda *et al.*, 2012], finite element model [e.g., Das *et al.*, 2013], and discrete element model [Wang *et al.*, 2008; Marketos and Bolton, 2009; Rahmati *et al.*, 2014]. In particular, the discrete element method [Cundall and Strack, 1979] has been demonstrated to be a good tool for simulating the micromechanics of compaction bands [e.g., Antonellini and Pollard, 1995; Rahmati *et al.*, 2014], because it permits large relative motion and dynamic evolution [e.g., Wang *et al.*, 2008]. In order to simulate the inelastic yielding of CBs, Wang *et al.* [2008] adapted a method introduced by Katsman *et al.* [2005], in which a discrete element shrinks when one of its normal contact stresses attains a critical value. Their simulation results indicate that the development of discrete compaction bands is promoted in a relatively homogeneous model [Wang *et al.*, 2008]. Three-dimensional bonded discrete element models have been used to simulate the generation and propagation of CBs [Marketos and Bolton, 2009; Dattola *et al.*, 2014] and drilling-induced compaction bands [Rahmati *et al.*, 2014], which provide new insights for the micromechanics of CBs.

One of the major objectives of this paper is to clarify the mechanism of the transition of compaction bands from chevron to wavy to straight CBs as documented in Figure 1a. In the companion paper [Liu *et al.*, 2015], petrographic analysis has shown that the shapes of wiggly CBs are correlated with the grain sorting and the porosity of sandstone. It is inferred that the yielding cap of rock is changed when these two factors vary, resulting in the different types of wiggly CBs. In this paper, an enhanced discrete element method is used to simulate the development of compaction bands. Elements in the model are close packed, and each element represents a pore structure, i.e., an assemblage of several rock grains. In correspondence with the yielding failure of sandstone, there is a yielding cap for the discrete elements. An element will be compacted (shrink) when the force state of one of its bonds reaches its yielding cap. A series of numerical simulations with different yielding caps of elements are carried out to investigate the mechanism of formation of wiggly CBs. The influences of cementation and yielding stress on the failure angle and the shapes of wiggly CBs are discussed. Finally, the petrophysical attributes and mechanical properties that influence the shape of wiggly CBs are addressed. In this study, the convention that compressive stresses are positive is used, and the maximum principal stress is represented by σ_1 .

2. The Discrete Element Model

2.1. Basic Discrete Element Model

The discrete element method (DEM) was first introduced by *Cundall and Strack* [1979] to study the behavior of granular assemblies. The method has been enhanced to a close-packed lattice solid model that was used in the simulation of the dynamical processes associated with earthquakes [*Mora and Place*, 1993, 1994]. Further, a bonded discrete element model was introduced to simulate the behaviors of cohesive materials [*Potyondy and Cundall*, 2004], e.g., soil and rock. The bonded lattice solid model has been applied in the investigation of the kinematic characteristics of structures [e.g., *Hardy and Finch*, 2006; *Yin et al.*, 2009].

In this study, the granular model is made up of a series of uniform discrete elements, which are close packed (hexagonal lattice) to represent a block of sandstone (Figure 2a). The elements of the model are bonded by breakable elastic springs (Figure 2b), and the spring force occurs only at contacts between neighboring elements. The normal spring force (F_n) between two elements is the product of the interelement stiffness (K_n) and the relative normal displacement (X_n). Elements are originally bonded to each other, until X_n reaches the breaking displacement (X_p), whereupon the bond breaks and the tensile force between them goes to zero.

The bonded model with a normal spring is similar to the spring network model, which has been used by *Katsman et al.* [2005] to simulate the formation of compaction bands. However, shear force and cohesion between elements are not considered in their model. In Figure 2c, a shear spring is used in this model to simulate the shear force between elements. Similar to the normal force, the shear spring force is the product of the shear stiffness (K_s) and the shear relative displacement (X_s). An initial shear resistance (F_{S0} , i.e., cohesion) exists between the elements, and the maximum shear force allowed by Coulomb friction is [*Liu et al.*, 2013]

$$F_{S\max} = F_{S0} + \mu_p F_n \quad (1)$$

where μ_p is the interelement coefficient of friction. The intact bond will break when the shear force exceeds $F_{S\max}$, and the maximum shear force of the broken bond ($F_{S\max}'$) reduces to $\mu_p \cdot F_n$ [*Hazzard et al.*, 2000]. When the bond is broken and the external shear force exceeds the limit $F_{S\max}'$, two elements start slipping relative to each other.

In numerical simulation, the resultant force acting on an element is the summation of the normal forces, shear forces, viscous force (see section 3.1), and gravity on the element. The dynamic evolution of the model can be simulated by integrating the equation of motion using Newtonian physics and a time-stepping algorithm [*Cundall and Strack*, 1979; *Potyondy and Cundall*, 2004; *Liu et al.*, 2013]. As the step time is very small, the acceleration of an element is assumed to be constant within a time step, which allows the calculation of velocity and displacement of each element.

2.2. Yielding Failure of Elements

The formation of compaction bands is associated with grain crushing and collapse of pore structures at the microscale. In discrete element models, there are several methods to simulate compaction failure. This process has been simulated by removing the elements [*Couroyer et al.*, 2000] or reducing the Young's modulus of the elements [*Marketos and Bolton*, 2009], when the stress acting on the elements exceeds a limit. Such methods oversimplify the evolution of damage, as the compaction bands may be stiffer at larger strains [*Wong and Baud*, 2012]. In other studies, the crushing behavior of rock grains was simulated via a cluster technique [*Ergenzinger et al.*, 2011], in which a rock grain is represented by an assemblage of discrete elements. Using a similar method, a broken element can be replaced by several smaller elements to simulate grain crushing [*Tsougui et al.*, 1999; *Marketos and Bolton*, 2009].

The method used in this study is an enhancement of that used by *Katsman et al.* [2005] and *Wang et al.* [2008], who simulate compaction by reducing the bond length by a small value when the normal contact stresses or forces reach critical values. The element (grain) crushing criterion was defined only in terms of contact forces acting on the element. Although the spatial distribution of the contact forces around the element could affect element crushing, previous simulation results [*Katsman et al.*, 2005; *Wang et al.*, 2008] have shown that different types of compaction bands can be simulated using the method.

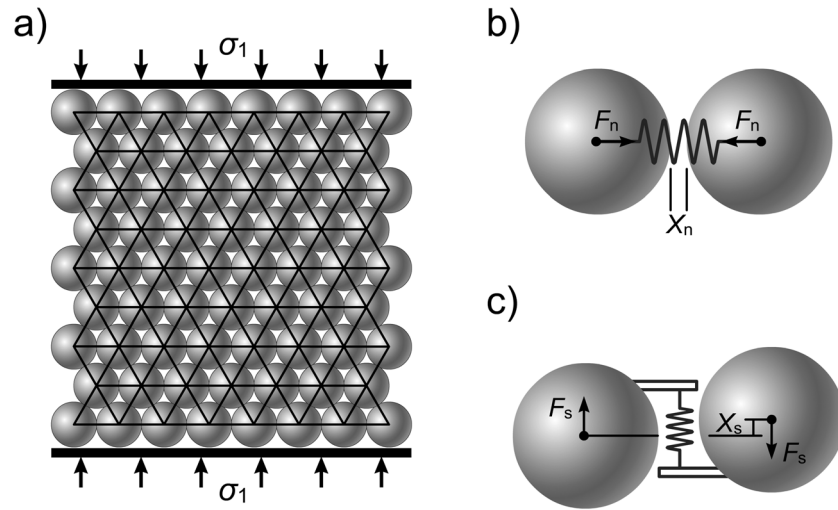


Figure 2. (a) A close-packed discrete element model. (b) Two elements are bonded by a breakable elastic spring along the normal direction and interact through a spring force (F_n). (c) Two elements also are bonded by a spring along the tangential direction to simulate the shear force (F_s). X_n is the relative normal displacement, and X_s is the relative shear displacement.

In correspondence with the cap model [Olsson, 1999; Issen and Rudnicki, 2000] that involves normal and shear stresses, the criterion of compaction is determined by both the normal and shear forces in this study. As shown in Figure 3a, an element does not correspond to a single grain of sandstone but represents a pore structure surrounded by several grains [Katsman *et al.*, 2005], i.e., an assemblage of grains. As shown in the schematic diagram of Figure 3a, the rock grains are bonded to each other to form a pore structure in the original assemblage, and the porosity is relative high. When the rock is compacted under high compressive stresses, the grains rearrange and the pore structure collapses, reducing the porosity of the assemblage. To simulate this compaction effect, under a certain force state, the original element is compacted and its radius is reduced. The mass of the compacted element remains constant, while its “porosity” reduces (Figure 3a). In addition to tensile and shear failure, a yielding criterion of discrete elements is used to simulate the collapse of pore structures. The yielding cap of an element (Figure 3b) is a portion of an ellipse defined by

$$F_n^2 + (F_s/k)^2 = F_f^2 \quad (2)$$

where F_n and F_s are, respectively, the normal and shear forces of a bond, k is the aspect ratio of the yielding ellipse, and F_f is the failure force, i.e., the maximum compressive force.

The failure criterion of an element can be described by a failure envelope of a bond, which is plotted in coordinates of F_s - F_n (Figure 3b). When $k = 1$, the failure envelope is defined by segments AB , BC , and arc CD . The interelement bond breaks in opening mode when the bond normal force exceeds the breaking force ($F_b = K_n \cdot X_b$). The onset of shear failure is demarcated by the straight line BC and is determined by equation (1). The onset of compaction yielding is indicated by the cap (arc CD). An element is compacted and shrinks when its force state reaches arc CD . As described in equation (2) and Figure 3b, the size of the cap ellipse is determined by the failure force, F_f , while the shape of the ellipse is determined by the aspect ratio, k . Different yielding caps can be obtained when k varies. Specifically, the compaction of an element is only determined by the normal force when $k = \infty$, and that is the failure criterion of element bonds used by Katsman *et al.* [2005] and Wang *et al.* [2008].

2.3. Micromechanical Parameters and Model Mechanical Properties

A Matlab code “MatDEM^{3D}” has been developed on the basis of the enhanced discrete element method, which considers the failures in tension, shear, and compaction. MatDEM^{3D} is a three-dimensional numerical code. Therefore, one layer of elements is used to investigate the two-dimensional behavior of compaction bands. The model geometry (Figure 4) used in this study is composed of bonded elements with identical size and mechanical parameters. The mean grain diameter of Aztec Aeolian sandstone is about 0.25 mm within a range of about 0.1 to 0.5 mm [Flodin *et al.*, 2005]. To represent a pore structure that is composed of several

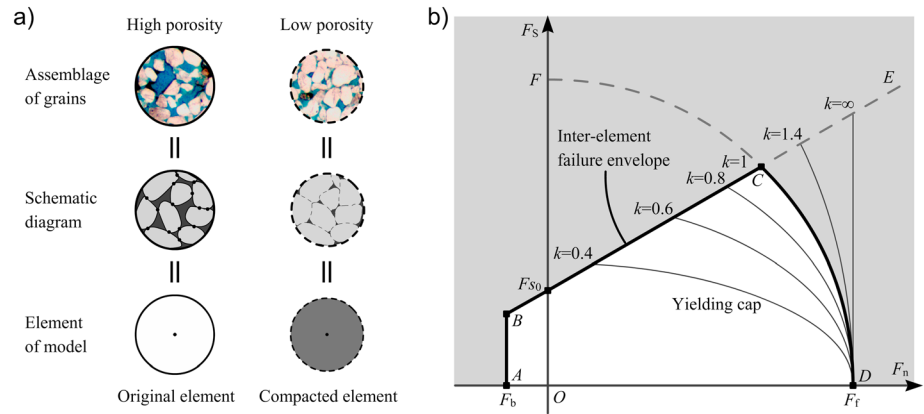


Figure 3. (a) A discrete element represents an assemblage of grains in porous sandstone. When the assemblage is compacted, its porosity and volume reduce. (b) Failure envelope of discrete element includes an elliptical yielding cap. An element will be compacted (shrink) when the force state of one of its bonds reaches the cap. F_f is the failure force; k is the aspect ratio of the yielding ellipse; F_b is the breaking force; and F_{S0} is the initial shear resistance (i.e., cohesion).

grains (Figure 3a), an element diameter of 1 mm is used. The model is bounded with rigid planes on its four sides. The planes are smooth, in which case there is no friction between the planes and the boundary elements. Discrete elements are close packed to form a hexagonal network, which is similar to the spring network model used by *Katsman et al.* [2005]. The model, 4.8 cm in width, 1.14 cm in height, and 1 mm in thickness, includes 618 elements.

Using this small model with a regular packing, we investigate mechanical factors that lead to different directions of segments of compaction bands, i.e., different failure angles. However, a larger model also is used to investigate the growth of compaction bands and the influences of model size on the results in section 3.5. Similar to the two-dimensional discrete element model [*Hardy and Finch*, 2006], the element mass (m) of the three-dimensional model is determined by

$$m = \rho \cdot (\sqrt{2}d^3 / 2) \tag{3}$$

where ρ is the density of sandstone ($2.25 \times 10^3 \text{ kg/m}^3$), d is the element diameter (0.001 m). According to the equation, the element mass is $1.591 \times 10^{-6} \text{ kg}$.

In order to investigate the influence of micromechanics on the formation of compaction bands, the interelement parameters must be chosen according to the mechanical properties of the sandstone. The regular packing model has analytical solutions between the interelement mechanical parameters and the model mechanical properties [*Liu et al.*, 2013]. As described in the previous section, the discrete element model involves the following five independent interelement parameters: K_{nr} , K_{sr} , χ_b , F_{S0} , and μ_p . Similar to the method of *Liu et al.* [2013], the conversion formulas between mechanical properties of rock and interelement parameters of three-dimensional discrete elements have been derived and are given in Appendix A. Using these formulas, the five interelement parameters can be determined by five mechanical properties of sandstone: Young's modulus (E), Poisson's ratio (ν), tensile strength (T_u), compressive strength (C_u), and coefficient of intrinsic friction (μ_i). Table 1 gives the initial mechanical properties of the sandstone [*Bieniawski*, 1984] and the calculated interelement mechanical properties. Mechanical properties of the close-packed model determined by the conversion formulas are

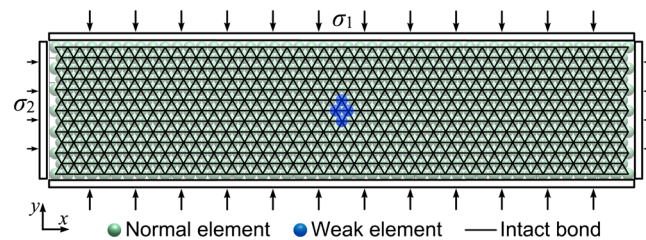


Figure 4. The close-packed model with size 4.80 cm \times 1.14 cm is bonded by four smooth planes. In numerical simulation, the model is compressed by the planes to generate compaction bands. Vertical compression is the maximum principle stress (σ_1); horizontal compression is σ_2 . Green color elements are regular elements, and central blue color elements are assigned 90% lesser failure force.

parameters of three-dimensional discrete elements have been derived and are given in Appendix A. Using these formulas, the five interelement parameters can be determined by five mechanical properties of sandstone: Young's modulus (E), Poisson's ratio (ν), tensile strength (T_u), compressive strength (C_u), and coefficient of intrinsic friction (μ_i). Table 1 gives the initial mechanical properties of the sandstone [*Bieniawski*, 1984] and the calculated interelement mechanical properties. Mechanical properties of the close-packed model determined by the conversion formulas are

Table 1. Initial Mechanical Properties of Sandstone [Bieniawski, 1984], Micromechanical Parameters, and Tested Mechanical Properties of Model When Element Diameter Is 0.001 m

Initial Mechanical Properties of Sandstone		Interelement Parameters		Tested Mechanical Properties of Model	
Young's modulus	15 GPa	Normal stiffness (K_n)	7.80×10^6 N/m	Young's modulus	9.73 GPa
Poisson's ratio	0.16	Shear stiffness (K_s)	1.34×10^6 N/m	Poisson's ratio	0.19
Uniaxial tensile strength	10 MPa	Breaking force (F_b)	3.19 N	Uniaxial tensile strength	5.50 MPa
Uniaxial compressive strength	180 MPa	Shear resistance (F_{S0})	13.18 N	Compressive strength ^a	118.51 MPa
Coefficient of intrinsic friction	1	Friction coefficient (μ_p)	0.3964	Coefficient of intrinsic friction	1.003
		Failure force (F_f)	26.36 N	Yielding stress ^a	39.23 MPa

^aYielding failure is disabled in the test of uniaxial compressive strength. Yielding stress is tested when the lateral planes are fixed.

generally a bit lower than the theoretical values [Liu *et al.*, 2013]. Therefore, the model was compressed or extended to test the effective mechanical properties. The tested values are given in Table 1. The detailed processes and calculation methods of the model mechanical properties can be found in Liu *et al.* [2013].

According to the conversion formulas, interelement normal and shear stiffness are determined by Young's modulus and Poisson's ratio. Experiment data [Bieniawski, 1984] for E of sandstone ranges from 10 to 46 GPa with an average of 22 GPa, while ν ranges from 0.1 to 0.4 with an average of 0.2. Sternlof *et al.* [2005] tested the apparent Young's modulus of samples collected near Silica Dome from the results of triaxial compression tests. The tested values are 16.5 and 21.0 GPa at the confining pressures of 10 and 50 MPa, respectively. They estimated a lithostatic paleostress of 30 MPa. Therefore, a Young's modulus of 20 GPa and a Poisson's ratio of 0.2 were used in their model. More recently, Deng *et al.* [2015b] tested the Young's modulus of sandstone samples from the Valley of Fire. They measured E from 4.8 GPa to 6.5 GPa at a confining pressures ranging from 10 to 30 MPa. In this study, an intermediate Young's modulus 15 GPa is used in the conversion formulas, and the tested E (9.73 GPa) is between the measured values given by Deng *et al.* [2015b] and Sternlof *et al.* [2005]. A Poisson's ratio of 0.16 is used in the conversion formulas, and the tested Poisson's ratio of the model is 0.19.

In Table 1, the tested effective tensile strength (5.50 MPa) and the compressive strength (118.51 MPa) are close to the mean values of published data, 5 MPa and 96 MPa, respectively [Bieniawski, 1984]. Interelement coefficient of friction (μ_p) controls the slope of the Mohr-Coulomb failure envelope of the model [Boutt and McPherson, 2002]. The μ_p used in the model is 0.3964, smaller than the value used in the previous models, e.g., $\mu_p = 0.5$ [Wang *et al.*, 2008; Marketos and Bolton, 2009] and $\mu_p = 1.5$ [Rahmati *et al.*, 2014]. However, the tested coefficient of intrinsic friction (μ_i) of this model is 1.003, because the close-packed geometry will lead to a greater overall μ_i .

Via calibration, a failure force $F_f = 2 \cdot F_{S0}$ (26.36 N) is used. When an element is compacted, its radius is reduced by a constant value of $\varepsilon \cdot R$ (R is the element radius). Previous study has shown that compaction localization forms and propagates only if there is a drastic reduction of stress on a compacted element [Wang *et al.*, 2008]. Therefore, in their model Wang *et al.* adopted a value of 0.01 reduction of element radius when the element is compacted. A much greater ratio $\varepsilon = 0.1$ was used by Katsman *et al.* [2005]. By using these values, stresses between an element and its adjacent elements reduce to zero immediately when the element is compacted, which promotes the propagation of pore collapses [Wang *et al.*, 2008]. In this study, a lower ε of 0.005 is used, and the radius of an element is reduced by 2.5×10^{-6} m during compaction, which results in a reduction of 19.50 N in interelement normal force (F_n). This value is a bit lower than the interelement failure force (26.36 N). Therefore, the normal force between a newly compacted element and its adjacent element is not always zero but may be a value lower than 6.86 N. Because a collapsed pore structure may have a residual strength, a lower ε of 0.005 is used in the model. In order to investigate the growth of compaction bands, the elements are allowed to compact only two times.

In order to remain consistence with the conventions of the discrete element method, forces are used to describe the failure criterions instead of stresses. The forces can be divided by effective area to calculate stresses and be compared with the values used in some previous studies. As the effective area (A_e) of a three-dimensional element is $0.7954 \times 10^{-6} \text{ m}^2$ ($\pi \cdot d^2/4$), the cohesion ($F \cdot F_{S0}/A_e$) is 16.78 MPa, and the interelement tensile strength (cement strength, F_b/A_e) is 4.06 MPa. The element yielding strength (F_f/A_e) is 33.56 MPa. Wang *et al.* [2008] used greater strengths for elements, e.g., tensile and shear bond strength of 100 MPa, and

intragranular failure stress of 200 MPa. This difference is justified because an element represents a pore structure, which is less stiff than the grain elements used in the Wang et al. model. The mechanical properties of the elements are close to those used by *Marketos and Bolton* [2009]. Both normal and shear stiffness are 4×10^6 N/m in their three-dimensional model, and the element yielding strength is 40 MPa.

3. Numerical Simulations of Formation of Wiggly Compaction Bands

The interelement mechanical parameters in Table 1 are applied to the model elements shown in Figure 4. The numerical model with these mechanical parameters is called the *original model*. In this section, the original model is used to simulate the generation and propagation of compaction bands. In section 4, the interelement failure force and/or breaking force are doubled to investigate the influences of yielding stress and cement strength on the formation of wiggly CBs.

3.1. The Numerical Simulation

Discrete element numerical simulation is a dynamic process; the displacement of boundaries and failure of elements lead to wave propagation in the model. Seismic waves are attenuated, for example, by friction and scattering, as they travel through rocks [*Hazzard et al.*, 2000]. Therefore, an artificial viscosity (F_v) is used to dissipate kinetic energy in the numerical model. The viscous force is proportional to the element velocity and is defined by [*Place et al.*, 2002; *Finch et al.*, 2003]

$$F_v = -\eta \cdot x' \quad (4)$$

where η is viscosity, and x' is element velocity. In numerical simulations, a viscosity of 0.5023 N s/m is used to damp the dynamic waves. Numerical tests show that the kinetic energy of the model reduces rapidly using this viscosity.

The four boundaries are moved toward the model center step by step, to simulate the tectonic loading process. Stresses on boundary elements may increase significantly during a single step. In order to reduce this stress increase, the boundary displacements must be very small. In each compressive step, the displacements of the left and right planes (6.13×10^{-10} m) are 30% of that of the top and bottom planes (2.04×10^{-9} m), so the maximum compressive stress (σ_1) is vertical.

Detailed observations of compaction bands indicate that a compaction band initiates at a grain-scale flaw [*Sternlof et al.*, 2005], which collapses in response to the compressive stress. In Figure 4, four elements in the center of model are set as the “seed” of compaction bands and are assigned 90% lesser failure force. When the model is compressed, a compaction band starts from the seed. The step time of the simulations is 4×10^{-8} s. After each compressive step, the model is run for 50 time steps to dissipate the seismic waves. To generate compaction bands, the models are compressed by 18,000 steps. Discrete element numerical simulation generally involves a huge calculation. The numerical simulations were run using a quad-core CPU workstation, which has a peak performance of about 48 billion floating point operations per second. A simulation of the small model takes about 1 h. For the large model with 2579 elements, the simulation was run for 3.1×10^4 compressive steps and a total of 3.1×10^6 iterations, which took about 16 h.

3.2. Simulation Results With Different Yielding Caps

Three yielding caps with different aspect ratios (k), 0.5, 1, and 2 are used to define the failure behaviors of three models (Figure 5a). The simulation results of the models are shown in Figures 5b–5d. The light green balls in the figures are the original intact elements, and the red balls are the compacted elements. The compaction bands initiate at the model center. Depending on the aspect ratio of yielding ellipse, a compaction band may propagate perpendicular to or inclined to σ_1 . As both the models and the applied strains are symmetrical, the compaction bands in the models also are symmetrical.

When $k=0.5$ (Figure 5b), the compaction band propagates horizontally and perpendicular to σ_1 , which corresponds to straight T3₃ CBs (e.g., Figure 1a). When $k=2$ (Figure 5d), the compaction band propagates along 45° inclined directions. It may represent the shear-enhanced CBs that are inferred to form at 38–53° to σ_1 [*Eichhubl et al.*, 2010]. The compaction band switches to another 45° inclined direction, when it reaches the boundaries. Therefore, it shows a chevron pattern with sharp 90–100° corners and straight “limbs,” which is comparable to the chevron T3₁ CBs (e.g., Figure 1a).

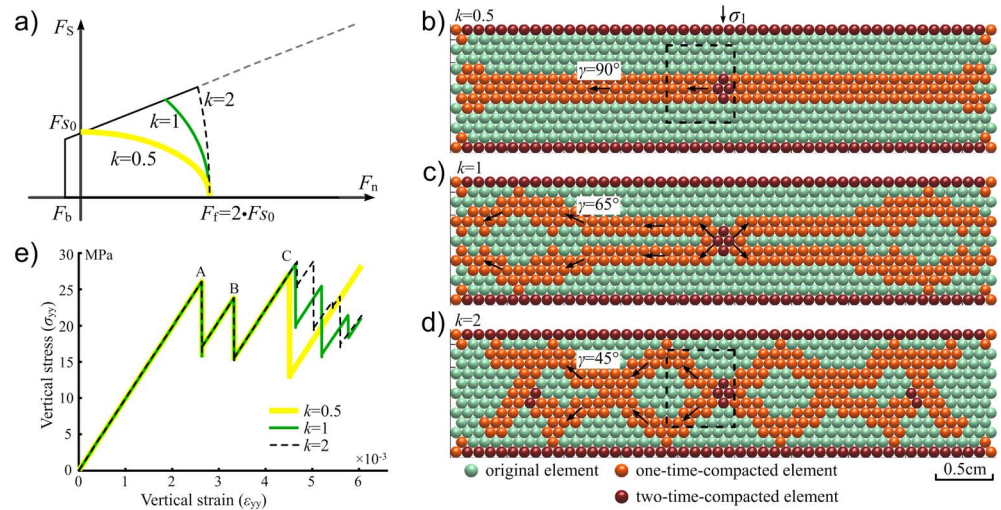


Figure 5. (a) Inter-element failure envelope when $F_f = 2 \cdot F_{S0}$. Failure caps defined by the aspect ratios $k = 0.5, 1, 2$ are assigned to models in Figures 5b–5d, respectively. (b–d) Simulation results when $k = 0.5, 1, 2$. When k is 0.5, the compaction band is straight and perpendicular to σ_1 ; when k is 2, the band alternates between two inclined directions and takes on a chevron shape; when k is 1, the band varies between straight and wavy shapes. The failure angle (γ) between σ_1 and band segment decreases with increasing k from Figures 5b–5d. (e) Vertical stress versus strain curves of the three models.

When an intermediate aspect ratio $k = 1$ is used, the compaction band may vary between wavy shape and straight shape. In Figure 5c, the compaction band propagates along inclined directions at the model center and then changes to the horizontal direction. The two horizontal compaction bands do not influence each other and propagate by approximately 1.5 cm. Subsequently, the compaction band is changed into a wavy shape (T3₂) that propagates along a 25° inclined direction; i.e., the failure angle (γ) between σ_1 and the band segment is 65°. From Figure 5b to Figure 5d, with the increasing k , the failure angle decreases from 90° to 45°.

Vertical stress-strain curves during the simulations are provided in Figure 5e. Although the boundary displacements are very small in each compressive step, the forces on boundary elements jump when the model is compressed. Due to the damping viscosity, the fluctuations of forces on internal elements are much smaller. As a result, these boundary elements compact prior to the internal elements [Marketos and Bolton, 2009]. In Figure 5e, the stress drops at points A and B correspond to the first and second compactions of boundary elements, respectively. The critical stress for onset of the central compaction band is approximately 28 MPa in Figure 5e. The critical stress is within the range of maximum compressive stresses estimated by Eichhubl et al. [2010] (20 MPa) and Sternlof et al. [2005] (40 MPa). It is smaller than the yielding stress of the model (39.23 MPa), as the stress concentrates around the central weak elements, which promotes the initiation of compaction bands. Based on a structural-diagenetic reconstruction of paleofluid flow in the Aztec Sandstone, Eichhubl et al. [2010] concluded that the compaction bands formed under an effective vertical stress (i.e., minimum compressive stress) of 10 MPa. In the simulations, the minimum compressive stress (horizontal) is 9.4 MPa when the compaction bands start to propagate.

3.3. Stress State and Force State of Band Tip During Compaction

Pure compaction bands (i.e., straight T3₃ CBs) have been interpreted by Sternlof et al. [2005] using an anticrack model [Fletcher and Pollard, 1981]. Compaction bands can be idealized as highly eccentric ellipsoidal bodies and can be represented mechanically as Eshelby inclusions that generate near-tip compressive stress concentrations [Sternlof et al., 2005]. Therefore, it is reasonable to postulate that the pure compaction bands propagate perpendicular to the direction of local maximum compressive stress [Meng and Pollard, 2014].

The sum of Y components (vertical) of bond forces divided by the effective element area is defined as σ_{yy} of an element. Figures 6a and 6b show σ_{yy} with $k = 0.5$ during propagation. Compaction bands in the figures are outlined by thick dashed lines. When the central elements are compacted, the stress is redistributed to the elements around them, which may be compacted subsequently. Therefore, the compaction band propagates horizontally, perpendicular to σ_1 , which is consistent with the results predicted by the anticrack model.

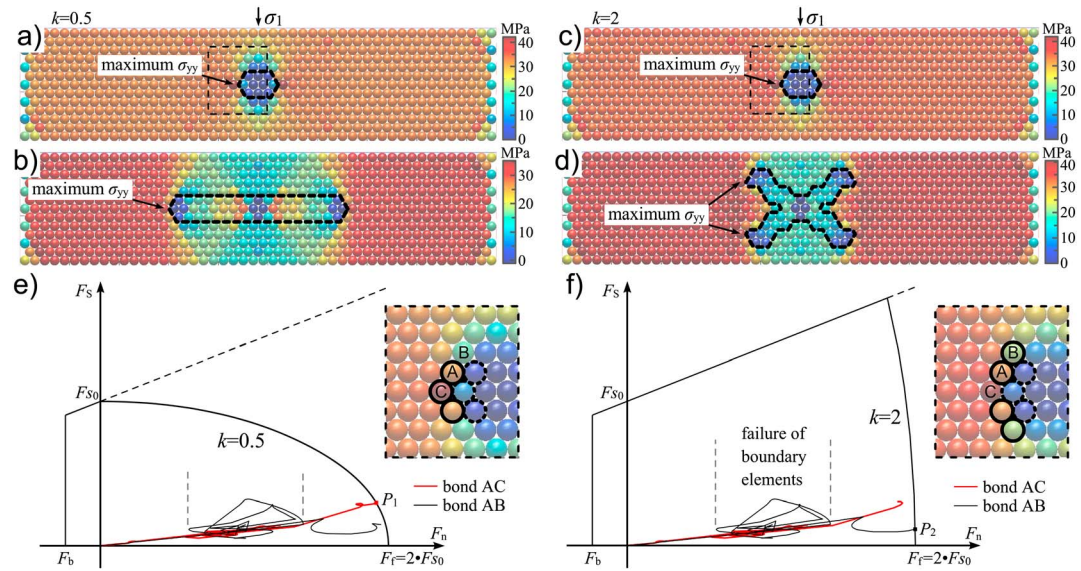


Figure 6. Stress component σ_{yy} as compaction bands propagate. Compaction bands are outlined by thick dashed lines. (a and b) $k = 0.5$; (c and d) $k = 2$. (e and f) Variation of force states of bonds when $k = 0.5$ and $k = 2$. Inset is the dashed region of Figures 6a and 6c, respectively. Curves of force states are almost the same in the two graphs. However, yielding failure may occur between bonds AC or AB when the shape of the yielding cap is different, which results in different directions of compaction band propagation.

However, discrete element simulation is a dynamic process (step by step), and an element will be compacted immediately when its force state exceeds the limit. Therefore, the concentration of stress in Figures 6a and 6b is not as significant as that predicted by the anticrack model [Rudnicki, 2007], which is based on a continuum mechanics formulation. Figures 6c and 6d show the stress distribution with $k = 2$, when the compaction band propagates along inclined directions. The stress distribution of Figure 6c is almost the same as that of Figure 6a (with $k = 0.5$), and the maximum σ_{yy} also occurs at elements adjacent to the band tip. As can be seen in Figure 6d, however, compaction bands propagate along inclined direction. These results indicate that the direction of compaction bands is not always determined by and perpendicular to σ_1 ; it is also influenced by the yielding cap of sandstone.

Propagation of compaction bands depends upon the failure process of the band tip elements. Elements around the band tips in Figures 6a and 6c are drawn in Figures 6e and 6f, respectively. The elements marked by dashed circles are compacted first when the compaction band propagates, and the compressive forces are redistributed to surrounding elements A, B, and C. The critical force state may occur in bond AB when $k = 2$ or bond AC when $k = 0.5$. The curves of force states of bonds AB and AC are illustrated in the F_s - F_n graphs Figures 6e and 6f, respectively. As boundary elements are compacted one by one before the propagation of the central compaction band, force increases and drops within the range of the two vertical dashed lines. The curves of force states in the two figures are very close to each other. However, the yielding cap is curved toward the negative direction of the horizontal axis in Figure 6e ($k = 0.5$), so the force state of bond AC reaches the cap first. The yielding cap is almost vertical in Figure 6f ($k = 2$), so the force state of bond AB reaches the cap first. Therefore, failure of elements may occur along different directions when the yielding cap is different. Similarly, when a pore structure of porous sandstone collapses and is compacted, the sequential compaction may be perpendicular to or inclined to σ_1 , depending on the mechanical properties and yielding caps of surrounding pore structures.

3.4. Transition Between Chevron, Wavy, and Straight CBs

In Figure 1a, the band type varies continually from chevron to wavy to straight CBs. Because the failure angle of model compaction bands is controlled by the yielding cap of elements, it is inferred that the transition of band shapes in outcrop is derived from the variation of yielding caps. To support this inference, the propagation of compaction bands in models with spatially variable yielding caps is simulated. In Figure 7a, the aspect ratio of the yielding ellipse decreases from 2 at the center to 0.5 at the lateral sides. The models are

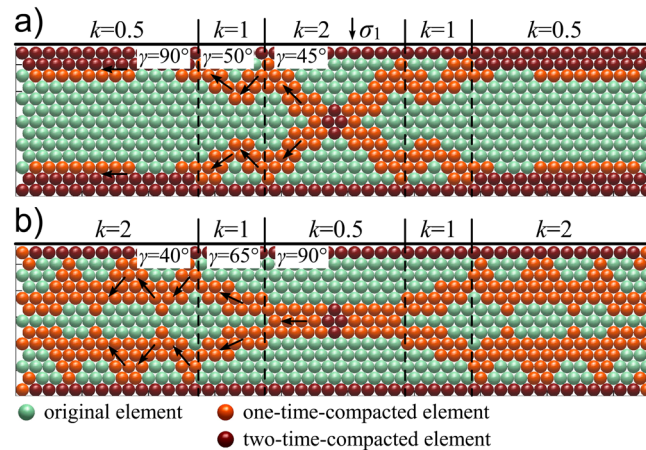


Figure 7. (a) Failure angle (γ) between σ_1 and band segment increases from 45° to 90° , where the aspect ratio (k) of yielding ellipse decreases from 2 at the center to 0.5 toward the lateral sides. The model compaction bands vary from chevron shape to straight, which is similar to the transition of band shape in Figure 1a. (b) The compaction band varies from straight to wiggly shape, when the spatial variation of k is reversed.

and the shape of the compaction bands depend on the yielding caps of the elements. We suggest that variations of yielding cap also occur in the Aztec sandstone, which results in the continuous transition from chevron CB to straight CB as shown in Figure 1a. In the companion paper [Liu et al., 2015], thin section analysis of the rock samples drilled at the site of Figure 1a also shows that the host rock of the straight CB have greater porosity and better sorting than that of the chevron CB. These results and the correlations are discussed in section 4.1.

3.5. Growth of Straight CB (T3₃) and Wavy CB (T3₂)

In the simulations of the small model, the compaction band reflects from the boundary to form a chevron or wavy pattern (Figures 5c and 5d). However, there are no such boundaries that limit the propagation of the CBs in real sandstone (e.g., Figure 1a). It is possible that the shear-enhanced CBs switch their directions when they propagate a certain distance. Therefore, a larger model is used to investigate the propagation and thickening process of compaction bands. The setup of the model is the same as that of the model of Figure 4, but the size is doubled. Similar to the smaller model, three seed elements in the model center are assigned a 90% lesser failure force. The model is compressed step by step, and the horizontal displacement is 30% of the vertical displacement in each compressive step. Numerical simulations with two values, $k = 0.5$ and $k = 2$, were carried out, and the results are given in Figures 8a–8c and 8d–8f, respectively.

The straight T3₃ CB propagates perpendicular to σ_1 when $k = 0.5$. Figure 8a shows σ_{yy} of the model when the compaction band has propagated 1.7 cm from the central seed. The compaction band is outlined by thick dashed line. The elements in the model can be compacted by two times. As shown in Figure 8a (also Figure 8d), the stresses on the compacted elements are uneven. With increasing compression, the compacted elements and surrounding original elements may be compacted due to the concentrations of bond forces. In Figure 8b, elements are compacted beside the compaction band, which gets thicker gradually (Figure 8c). Furthermore, secondary compactions occur in the CBs (Figures 8c and 8f), reducing the “porosity” of CBs.

When $k = 2$ (Figures 8d–8f), the compaction band propagates from the central seed, along a 45° direction first, and then it gradually changes to another inclined direction as it propagates approximately 1.5 cm (Figure 8d). The CB continues propagating for approximately 2.5 cm as the band tip rotates gradually to another inclined direction. The geometry of the CB is very similar to the wavy T3₂ CBs observed in field (e.g., Figure 1b), which have straight limbs and somewhat rounded hinge. Furthermore, the compaction band may propagate along two inclined directions when it starts from the seed, which is similar to the result shown in Figure 5d. Therefore, the two directions are the predominant failure directions of bands when $k = 2$. However, in this simulation, the compaction band switches direction when it propagates by several centimeters and does not reach the boundaries. We assume that the force states (also stress) of tip elements

compressed step by step according to the process introduced in section 3.1. The compaction band first propagates along the 45° direction in the central area (with $k = 2$), which is the same as Figure 5d. In the region of $k = 1$, the failure angle between band segment and σ_1 increases a bit to approximately 55° . Finally, when $k = 0.5$, the compaction band propagates along the model boundaries and perpendicular to σ_1 . The simulation result is comparable to the variation of wiggly CBs in Figure 1a.

In Figure 7b, the failure angle (γ) decreases from 90° at the central area where $k = 0.5$, reduces to 65° when $k = 1$, and to 40° when $k = 2$. The compaction band varies from a planar shape at the center to a wiggly shape at the lateral sides. Therefore, the failure angle

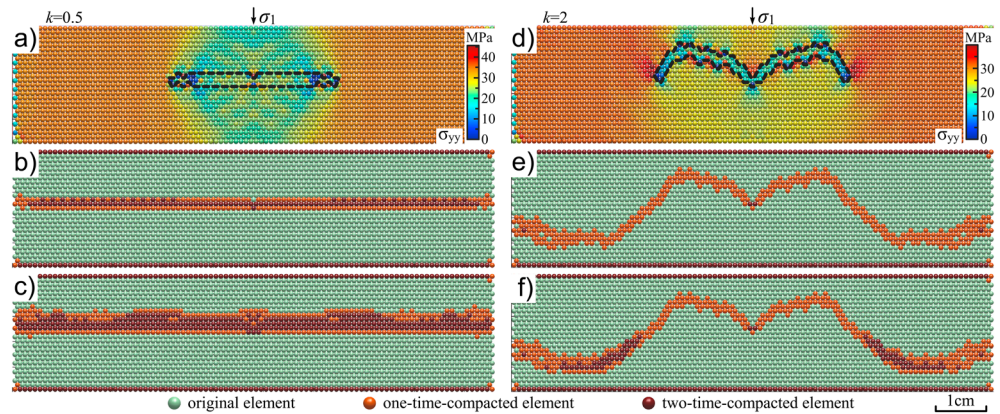


Figure 8. Simulation results of a model with size 9.6 cm × 2.35 cm. Three weak elements in the model center are the “seed” for the model compaction bands. (a–c) Growth of CB band when $k = 0.5$. (d–f) Growth of a wavy CB when $k = 2$. Figures 8a and 8d show the distribution of σ_{yy} ; CBs are outlined by dashed lines.

vary when the inclined band propagates. The variation of force states exceeds a limit when the length of band segment reaches a critical value, and the band direction alternates. Such transition occurs every several centimeters, and as a result, wiggly CBs alternate direction between two predominant inclined directions and show chevron or wavy shapes.

4. Discussion: Factors Influencing Wiggly Band Geometry

4.1. Yielding Cap and Failure Angle

Studies of rock samples [Schultz *et al.*, 2010; Fossen *et al.*, 2011; Cheung *et al.*, 2012] and laboratory experiments on porous rock [Klein *et al.*, 2001; Baud *et al.*, 2004] have shown that grain sorting and porosity are key petrophysical attributes that can control the formation of compaction bands in porous sandstone. In the companion paper [Liu *et al.*, 2015], petrographic analyses of thin section images indicate the sorting degree and porosity of the host rock increase from chevron ($T3_1$) to wavy ($T3_2$) to straight CBs ($T3_3$). The failure angles of band segments of the three band types are approximately 90°, 65°, and 45° (e.g., Figure 1a), respectively. Therefore, it is inferred that the variation of band shape is due to the increasing failure angle of sandstone, which is related to the increasing sorting degree and porosity.

In the numerical simulations, compaction bands show a zigzag geometry that is similar to the wiggly CBs documented in outcrop. When the aspect ratio of yielding ellipse increases from 0.5 to 1 and 2, the failure angle of compaction bands decreases from approximately 90° to 65° and 45° (Figures 5b–5d), which is comparable to the straight CBs, wavy CBs, and chevron CBs. Particularly, when k varies from 2 at the center to 0.5 at the lateral sides of the model, the variation of chevron CBs to straight CBs is simulated. Therefore, we infer that porosity and grain sorting affect the mechanical properties of rock (e.g., effecting the yielding cap) and lead to different failure angles of band segments and different patterns of wiggly CBs. In addition, other microparameters, e.g., grain size, cementation and yielding stress also may have effects on the yielding cap of sandstone [see review of Wong and Baud, 2012]. Interelement mechanical parameters can be adjusted to investigate their influences on the failure angle and the shape of compaction bands.

4.2. Critical Yielding Stress

The critical yielding stress is primarily determined by the failure force of elements in this study. To investigate the influences of yielding stress on the formation of wiggly CBs, we double the failure force $F_f = 4 \cdot F_{50}$. In keeping with the greater failure force, the compressive step is doubled in these simulations, while other parameters of the simulations are the same as the original model. The results for models with the aspect ratios, 0.5, 1, and 2, are given in Figures 9b–9d. When $k = 0.5$, the compaction band propagates approximately 70° to σ_1 first and perpendicular to σ_1 later. When $k = 1$ and 2, the compaction bands are wiggly at approximately 45° and 40° to σ_1 . The failure angle also decreases with increasing k , but the values are less than those of the original model (Figures 5b–5d). Apparently, the model bands tend to be more inclined to σ_1 when the failure force (i.e., yielding stress) increases.

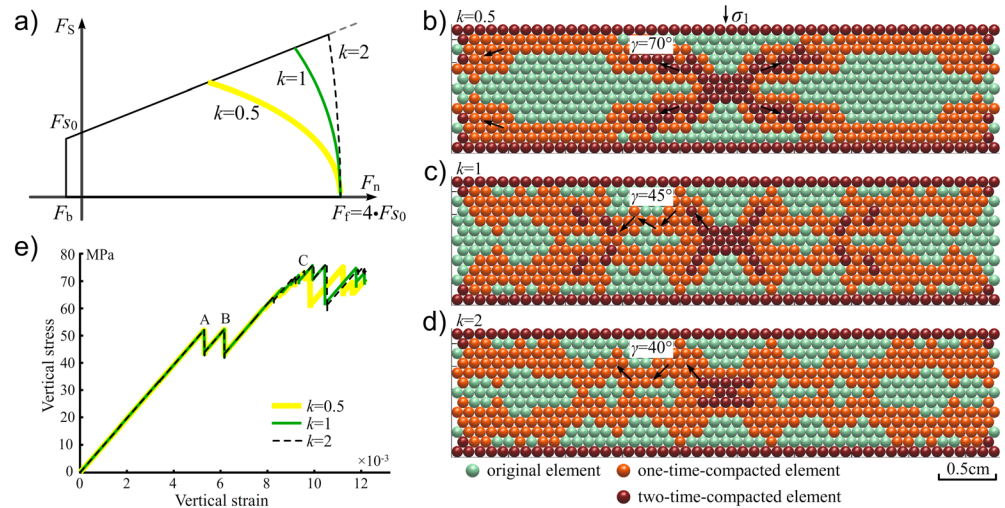


Figure 9. (a) Inter-element failure envelopes when failure force $F_f = 4 \cdot F_{S0}$. (b–d) Simulation results when $k = 0.5, 1, 2$. When k increases, the failure angle of band segment decreases, and the compaction band tends to be more wiggly. (e) Vertical stress versus strain curves of the three models.

Chevron CBs ($T3_1$) and straight CBs ($T3_3$) have different microstructures in the host rock. Navajo Sandstone in the Buckskin Gulch site [Fossen et al., 2011] shows that pure CBs (i.e., $T3_3$ CBs) only occur in the lower and most coarse grained and well-sorted parts of grain flow units. In the companion paper, petrographic analyses show that the host rock porosity of chevron CBs is less than that of straight CBs [Liu et al., 2015]. Because the yielding stress generally increases with decreasing porosity [Zhang et al., 1990; Wong and Baud, 2012], sandstone with lesser porosity generally has a greater yielding stress [Schultz et al., 2010]. The simulation results are consistent with the fact that straight $T3_3$ CBs form in high-porosity sandstone with lesser yielding stress, and chevron $T3_3$ CBs form in relative low porosity sandstone with greater yielding stress.

Curves of vertical stresses during compressions are shown in Figure 9e. The critical stress for the onset of central compaction band is approximately 63 MPa. The curves of different aspect ratios (k) are almost the same, although the shapes of the compaction bands are quite different. This indicates that the onset of collapse is determined by F_f , but it is not influenced significantly by k . The minimum compressive stress (horizontal) is approximately 20 MPa when the compaction bands start to propagate.

4.3. Cement Strength

The cementation of sandstone is represented in these models by interelement bonds, and the cement strength is determined by interelement breaking force (F_b). To investigate the influences of cement strength on the formation of compaction bands, numerical models with twice F_b are investigated. Failure envelopes for the models, and the results are given in Figures 10a–10c. When $k = 0.5$, the straight CB is almost the same as the result of the original model (Figure 5b). However, when $k = 2$, the compaction band still is perpendicular to σ_1 , while the CB is 45° inclined to σ_1 in Figure 5d (with original F_b). The results indicate that a higher strength of cement restrains chevron CBs (shear enhanced) and promotes straight CBs (pure compacted).

Microscopic observations have shown that shear fractures typically do not propagate in their own plane, and the eventual failure of rock samples occurs by linkage of tensile microcracks to form a macroshear fault [Horii and Nemat-Nasser, 1985; Moore and Lockner, 1995]. Discrete element numerical simulations have shown that tensile microcracks and grain crushing were pervasive inside the shear band [Wang et al., 2008, Figure 6b]. Boutt and McPherson [2002] also observed that models with a high ratio of shear to normal bond strength produce a well-defined shear plane. In these numerical simulations, most opening microcracks are associated with segments of wiggly CBs (shear enhanced). Therefore, we suggest that tensile microcracks also play an important role in the formation of shear-enhanced compaction bands. Since the greater strength of

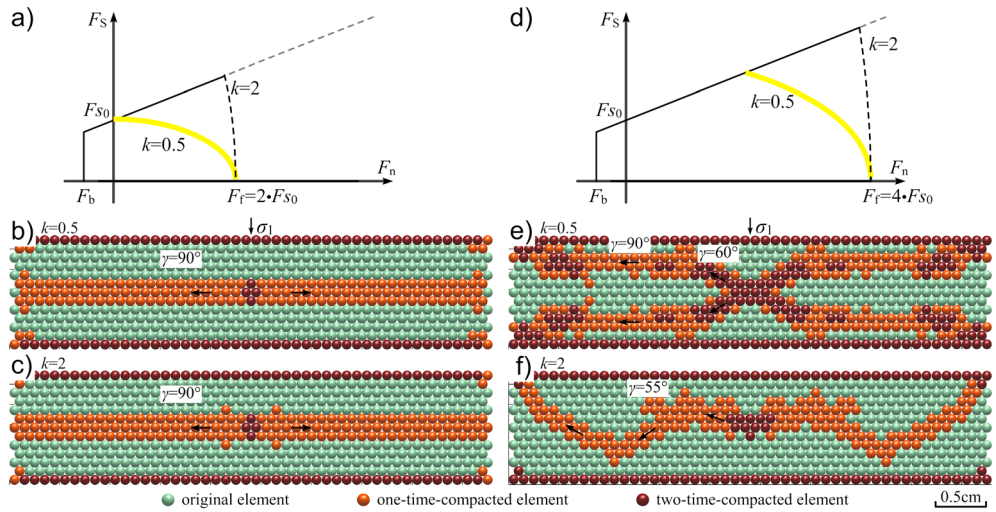


Figure 10. (a) Failure envelopes of elements in Figures 10b and 10c. (b and c) Simulation results of models with double F_b . Compaction bands are perpendicular to σ_1 ($\gamma = 90^\circ$), when $k = 0.5$ and $k = 2$. Therefore, greater F_b promotes straight T3₃ CBs. (d) Failure envelopes of elements in Figures 10e and 10f. (e and f) Compaction bands have lesser γ , when both F_b and F_f of model elements are doubled. Therefore, greater F_f promotes chevron T3₁ CBs and wavy T3₂ CBs.

cement restrains the onset of tensile microcracks, the compaction bands tend to be perpendicular to σ_1 when a greater F_b is used.

Figures 10e and 10f show the simulation results with double failure forces (F_f) and double breaking forces (F_b). The failure envelopes of the two models are given in Figure 10d. When $k = 0.5$, the compaction bands in Figure 10c are composed of segments of straight CBs and inclined shear-enhanced CBs, which have failure angles of 90° and 60° , respectively. When $k = 2$ (Figure 10f), the compaction bands show a wavy shape with a lower mean failure angle of approximately 55° . In comparison with Figures 9b and 9d (with original F_b), the CBs have greater failure angles, but the failure angles of the CBs are less than the straight T3₃ CBs in Figures 10b and 10c (with original F_f). The results indicate the failure angle of CBs is controlled by F_f and F_b , i.e., yielding stress and cement strength of sandstone. Greater F_f promotes chevron T3₁ CBs with lower failure angles, and greater F_b promotes straight T3₃ CBs with greater failure angles. It is inferred, therefore, that the ratio of interelement failure force to breaking force influences the shape of wiggly CBs. In the original model, the ratio of $F_b:F_{50}:F_f$ is about 1:4.1:8.2. The three interelement parameters correspond to three macromechanical properties of the original model, tensile strength (5.50 MPa), shear strength (24.49 MPa), and yielding stress (39.23 MPa); the ratio of the three properties is 1:4.5:7.1.

4.4. Stress and Heterogeneity

The numerical simulations indicate that the failure envelope has an important impact on the formation of wiggly CBs. However, we do not assume CB geometry is determined only by the mechanical properties of sandstone. Numerical simulations with different lateral stresses (range from 8 MPa to 70 MPa) have been investigated by Wang *et al.* [2008]. Their simulation results show that the damage distribution is more diffuse and delocalized at higher lateral stresses. In the numerical simulations of the current study, the ratio of the maximum compressive stress (e.g., $\sigma_1 = 28$ MPa) to minimum principle stress (e.g., $\sigma_2 = 9.4$ MPa) is approximately 3:1. Variation of lateral stress (σ_2) and the ratio of σ_1 to σ_2 may influence compaction band geometry, and this will be analyzed in future work.

Numerical simulations in previous studies [Katsman *et al.*, 2005; Wang *et al.*, 2008] indicate that the discrete compaction bands are promoted in a relatively homogeneous granular aggregate, and diffuse bands and distributed cataclastic flow usually form in a more heterogeneous model. Therefore, the formation of compaction bands also is influenced by the distribution of element mechanical properties. In this study, all the elements (except the central elements) are assigned the same mechanical properties, and planar

compaction bands always form in the simulations. It is inferred that heterogeneity in the model may result in diffuse bands and distributed cataclastic flow, but this requires further modeling, data gathering, and thin section analyses that are beyond the scope of this paper.

5. Conclusions

Wiggly compaction bands (T3) formed in porous sandstone may vary from chevron shape (T3₁) to wavy shape (T3₂) to nearly straight (T3₃). In this study, an enhanced discrete element method is used to investigate the mechanisms of formation of wiggly CBs in porous sandstone. Simulation results for the original models show that compaction bands vary from straight to chevron shape when the aspect ratio (*k*) of the yielding ellipse increases from 0.5 to 2. This shape variation corresponds to a decrease of failure angle from approximately 90° to 45°. Analysis of force states adjacent to tip elements show that the different failure angles are due to different yielding caps. When *k* is 0.5 and 2, sequential compaction occurs along the horizontal direction and inclined direction, respectively. Similarly, when a pore structure of porous sandstone is compacted, the sequential compaction may be perpendicular to or inclined to σ_1 , depending on the yielding caps of the surrounding pore structures. As host rock porosity and sorting degree of chevron CBs is lower than that of straight CBs [Liu et al., 2015], we infer that the petrophysical attributes influence the mechanical properties of rock (e.g., yielding cap) and result in different failure angles of band segments and different patterns of wiggly CBs.

Propagation of compaction bands in the larger models provides important clues for the development of CBs. With increasing compressive strain, stresses concentrate on compacted elements and adjacent elements, which result in secondary compaction and thickening of CBs. When *k*=2, the compaction bands alternate direction when they propagate by approximately 3 cm, almost the same as the wavy CBs observed in the field [Liu et al., 2015]. Apparently, the variation of force states of tip elements exceeds a limit when the band segment propagates by several centimeters. As a result, the band direction alternates between two predominant inclined directions and shows a chevron or wavy shape.

The simulations highlight the influences of critical yielding stress and cement strength on the formation of wiggly CBs. A greater critical yielding stress promotes chevron CBs (shear-enhanced), and a greater strength of cement promotes straight CBs (pure compacted). Thus, the ratio of cement strength to critical yielding stress provides a quantitative rationale for the different shapes of wiggly CBs. Combined with the petrographic analysis introduced in the companion paper [Liu et al., 2015], we conclude that the patterns of wiggly CBs are controlled by the mechanical properties of sandstone, in particular, the shape of the yielding cap, the critical yielding stress, and the cement strength. These mechanical properties are mainly determined by petrophysical attributes, e.g., grain sorting, porosity, and cementation.

Appendix A

Interelement normal stiffness (K_n), shear stiffness (K_s), breaking force (F_b), initial shear resistance (F_{s0}), and coefficient of friction (μ_p) can be defined by five mechanical properties of sandstone, including Young's modulus (E), Poisson's ratio (ν), tensile strength (T_u), compressive strength (C_u), and coefficient of intrinsic friction (μ_i):

$$K_n = \frac{\sqrt{2}Ed}{4(1-2\nu)} \tag{A1}$$

$$K_s = \frac{\sqrt{2}(1-5\nu)Ed}{4(1+\nu)(1-2\nu)} \tag{A2}$$

$$F_b = \frac{3K_n + K_s}{6\sqrt{2}(K_n + K_s)} \cdot T_u \cdot d^2 \tag{A3}$$

$$F_{s0} = \frac{1 - \sqrt{2}\mu_p}{6} \cdot C_u \cdot d^2 \tag{A4}$$

$$\mu_p = \frac{-2\sqrt{2} + \sqrt{2}l}{2 + 2l}, \quad l = \left[(1 + \mu_i^2)^{1/2} + \mu_i \right]^2 \tag{A5}$$

Acknowledgments

Financial supports from the Department of Energy (DE-FG02-04ER15588), National Natural Science Foundation of China (41230636; 41302216) and Natural Science Foundation of Jiangsu province (BK20130377) are gratefully acknowledged. We are grateful to anonymous reviewers for many valuable comments that notably improved the manuscript. Data used in this paper is available online: <http://acei.cn/program/WigglyCB>.

References

- Antonellini, M. A., and D. D. Pollard (1995), Distinct element modeling of deformation bands in sandstone, *J. Struct. Geol.*, *17*(8), 1165–1182, doi:10.1016/0191-8141(95)00001-T.
- Aydin, A., R. Borja, and P. Eichhubl (2006), Geological and mathematical framework for failure modes in granular rock, *J. Struct. Geol.*, *28*(1), 83–98, doi:10.1016/j.jsg.2005.07.008.
- Baud, P., E. Klein, and T. Wong (2004), Compaction localization in porous sandstones: Spatial evolution of damage and acoustic emission activity, *J. Struct. Geol.*, *26*(4), 603–624, doi:10.1016/j.jsg.2003.09.002.
- Bieniawski, Z. T. (1984), *Rock Mechanics Design in Mining and Tunneling*, 272 pp., A. A. Balkema, Brookfield, Vermont.
- Boutt, D., and B. McPherson (2002), Simulation of sedimentary rock deformation: Lab-scale model calibration and parameterization, *Geophys. Res. Lett.*, *29*(4), 1054, doi:10.1029/2001GL013987.
- Chemenda, A. I. (2009), The formation of tabular compaction-band arrays: Theoretical and numerical analysis, *J. Mech. Phys. Solids*, *57*(5), 851–868, doi:10.1016/j.jmps.2009.01.007.
- Chemenda, A. I. (2011), Origin of compaction bands: Anti-cracking or constitutive instability?, *Tectonophysics*, *499*(1–4), 156–164, doi:10.1016/j.tecto.2011.01.005.
- Chemenda, A. I., C. Wibberley, and E. Sallet (2012), Evolution of compactive shear deformation bands: Numerical models and geological data, *Tectonophysics*, *526–529*(2), 56–66, doi:10.1016/j.tecto.2011.10.003.
- Cheung, C., P. Baud, and T. Wong (2012), Effect of grain size distribution on the development of compaction localization in porous sandstone, *Geophys. Res. Lett.*, *39*, L21302, doi:10.1029/2012GL053739.
- Couroyer, C., Z. Ning, and M. Ghadiri (2000), Distinct element analysis of bulk crushing: Effect of particle properties and loading rate, *Powder Technol.*, *109*(1–3), 241–254, doi:10.1016/S0032-5910(99)00240-5.
- Cundall, P., and O. Strack (1979), A discrete numerical model for granular assemblies, *Geotechnique*, *29*(1), 47–65.
- Das, A., G. Nguyen, and I. Einav (2011), Compaction bands due to grain crushing in porous rocks: A theoretical approach based on breakage mechanics, *J. Geophys. Res.*, *116*, B08203, doi:10.1029/2011JB008265.
- Das, A., G. Nguyen, and I. Einav (2013), The propagation of compaction bands in porous rocks based on breakage mechanics, *J. Geophys. Res. Solid Earth*, *118*, 2049–2066, doi:10.1002/jgrb.50193.
- Dattola, G., C. di Prisco, I. Redaelli, and S. Utili (2014), A distinct element method numerical investigation of compaction processes in highly porous cemented granular materials, *Int. J. Numer. Anal. Methods Geomech.*, *38*(11), 1101–1130, doi:10.1002/nag.2241.
- Deng, S., L. Zuo, A. Aydin, J. Dvorkin, and T. Mukerji (2015a), Permeability characterization of natural compaction bands using core flooding experiments and three-dimensional image-based analysis: Comparing and contrasting the results from two different methods, *AAPG Bull.*, *99*(1), 27–49, doi:10.1306/07071413211.
- Deng, S., A. Cilona, C. Morrow, C. Mapeli, C. Liu, D. Lockner, M. Prasad, and A. Aydin (2015b), Cross-bedding related anisotropy and its interplay with various boundary conditions in the formation and orientation of joints in an aeolian sandstone, *J. Struct. Geol.*, *77*(8), 175–190.
- Eichhubl, P., J. Hooker, and S. Laubach (2010), Pure and shear-enhanced compaction bands in Aztec Sandstone, *J. Struct. Geol.*, *32*(12), 1873–1886, doi:10.1016/j.jsg.2010.02.004.
- Ergenzinger, C., R. Seifried, and P. Eberhard (2011), A discrete element model to describe failure of strong rock in uniaxial compression, *Granular Matter*, *13*(4), 341–364, doi:10.1007/s10035-010-0230-7.
- Finch, E., S. Hardy, and R. Gawthorpe (2003), Discrete element modelling of contractional fault-propagation folding above rigid basement fault blocks, *J. Struct. Geol.*, *25*(4), 515–528, doi:10.1016/S0191-8141(02)00053-6.
- Fletcher, R., and D. D. Pollard (1981), Anticrack model for pressure solution surfaces, *Geology*, *9*(9), 419–424, doi:10.1130/0091-7613(1981)9<419:AMFPSS>2.0.CO;2.
- Flodin, E. A., M. Gerdes, A. Aydin, and W. D. Wiggins (2005), Petrophysical properties and sealing capacity of fault rock from sheared-joint based faults, Aztec Sandstone, Nevada, in *Fault Seals and Petroleum Traps*, vol. 85, edited by Y. Tsuji and R. Sorkhabi, pp. 197–217, AAPG Mem., Tulsa, Okla.
- Fossen, H., R. Schultz, and A. Torabi (2011), Conditions and implications for compaction band formation in the Navajo Sandstone, Utah, *J. Struct. Geol.*, *33*(10), 1477–1490, doi:10.1016/j.jsg.2011.08.001.
- Hardy, S., and E. Finch (2006), Discrete element modelling of the influence of cover strength on basement-involved fault-propagation folding, *Tectonophysics*, *415*(1–4), 225–238, doi:10.1016/j.tecto.2006.01.002.
- Hazzard, J., R. Young, and S. Maxwell (2000), Micromechanical modeling of cracking and failure in brittle rocks, *J. Geophys. Res.*, *105*(B7), 16,683–16,697, doi:10.1029/2000JB900085.
- Hill, R. (1989), Analysis of deformation bands in the Aztec Sandstone, Valley of Fire State Park, Nevada, MS thesis, Univ. of Nevada, Las Vegas, Nevada.
- Horii, H., and S. Nemat-Nasser (1985), Compression-induced microcrack growth in brittle solids: Axial splitting and shear failure, *J. Geophys. Res.*, *90*(NB4), 3105–3125, doi:10.1029/JB090iB04p03105.
- Issen, K., and J. Rudnicki (2000), Conditions for compaction bands in porous rock, *J. Geophys. Res.*, *105*(B9), 21,529–21,536, doi:10.1029/2000JB900185.
- Issen, K., and J. Rudnicki (2001), Theory of compaction bands in porous rock, *Phys. Chem. Earth, Part A*, *26*(1–2), 95–100, doi:10.1016/S1464-1895(01)00031-X.
- Katsman, R., E. Aharonov, and H. Scher (2005), Numerical simulation of compaction bands in high-porosity sedimentary rock, *Mech. Mater.*, *37*(1), 143–162, doi:10.1016/j.mechmat.2004.01.004.
- Klein, E., P. Baud, T. Reuschle, and T.-f. Wong (2001), Mechanical behavior and failure mode of Bentheim sandstone under triaxial compression, *Phys. Chem. Earth, Part A*, *26*, 21–25, doi:10.1016/S1464-1895(01)00017-5.
- Liu, C., D. D. Pollard, and B. Shi (2013), Analytical solutions and numerical tests of elastic and failure behaviors of close-packed lattice for brittle rocks and crystals, *J. Geophys. Res. Solid Earth*, *118*, 71–82, doi:10.1029/2012JB009615.
- Liu, C., D. D. Pollard, S. Deng, and A. Aydin (2015), Mechanism of formation of wiggly compaction bands in porous sandstone: 1. Observations and conceptual model, *J. Geophys. Res. Solid Earth*, *120*, 8138–8152, doi:10.1002/2015JB012372.
- Marketos, G., and M. Bolton (2009), Compaction bands simulated in discrete element models, *J. Struct. Geol.*, *31*(5), 479–490, doi:10.1016/j.jsg.2009.03.002.
- Meng, C., and D. D. Pollard (2014), Eshelby's solution for ellipsoidal inhomogeneous inclusions with applications to compaction bands, *J. Struct. Geol.*, *67*, 1–19, doi:10.1016/j.jsg.2014.07.002.
- Mollema, P., and M. Antonellini (1996), Compaction bands: A structural analog for anti-mode I cracks in aeolian sandstone, *Tectonophysics*, *267*(1–4), 209–228, doi:10.1016/S0040-1951(96)00098-4.

- Moore, D., and D. Lockner (1995), The role of microcracking in shear-fracture propagation in granite, *J. Struct. Geol.*, *17*(1), 95–114, doi:10.1016/0191-8141(94)E0018-T.
- Mora, P., and D. Place (1993), A lattice solid model for the nonlinear dynamics of earthquakes, *Int. J. Mod. Phys. C*, *4*(6), 1059–1074, doi:10.1142/S0129183193000823.
- Mora, P., and D. Place (1994), Simulation of the frictional stick-slip instability, *Pure Appl. Geophys.*, *143*(1–3), 61–87, doi:10.1007/BF00874324.
- Olsson, W. (1999), Theoretical and experimental investigation of compaction bands in porous rock, *J. Geophys. Res.*, *104*(B4), 7219–7228, doi:10.1029/1998JB900120.
- Place, D., F. Lombard, P. Mora, and S. Abe (2002), Simulation of the micro-physics of rocks using LSMearth, *Pure Appl. Geophys.*, *159*(9), 1911–1932, doi:10.1007/s00024-002-8715-x.
- Potyondy, D., and P. Cundall (2004), A bonded-particle model for rock, *Int. J. Rock Mech. Min. Sci.*, *41*(8), 1329–1364, doi:10.1016/j.ijrmms.2004.09.011.
- Rahmati, H., A. Nouri, D. Chan, and H. Vaziri (2014), Simulation of drilling-induced compaction bands using discrete element method, *Int. J. Numer. Anal. Methods Geomech.*, *38*(1), 37–50, doi:10.1002/nag.2194.
- Rudnicki, J. (2004), Shear and compaction band formation on an elliptical yield cap, *J. Geophys. Res.*, *109*, B03402, doi:10.1029/2003JB002633.
- Rudnicki, J. W. (2007), Models for compaction band propagation, *Geol. Soc. London Spec. Publ.*, *284*(1), 107–125, doi:10.1144/SP284.8.
- Schultz, R., C. Okubo, and H. Fossen (2010), Porosity and grain size controls on compaction band formation in Jurassic Navajo Sandstone, *Geophys. Res. Lett.*, *37*, L22306, doi:10.1029/2010GL044909.
- Sternlof, K., J. Chapin, D. D. Pollard, and L. Durlinsky (2004), Permeability effects of deformation band arrays in sandstone, *AAPG Bull.*, *88*(9), 1315–1329, doi:10.1306/032804.
- Sternlof, K., J. Rudnicki, and D. D. Pollard (2005), Anticrack inclusion model for compaction bands in sandstone, *J. Geophys. Res.*, *110*, B11403, doi:10.1029/2005JB003764.
- Tsounghi, O., D. Vallet, and J. Charmet (1999), Numerical model of crushing of grains inside two-dimensional granular materials, *Powder Technol.*, *105*(1–3), 190–198, doi:10.1016/S0032-5910(99)00137-0.
- Wang, B., Y. Chen, and T. Wong (2008), A discrete element model for the development of compaction localization in granular rock, *J. Geophys. Res.*, *113*, B03202, doi:10.1029/2006JB004501.
- Wong, T., and P. Baud (2012), The brittle-ductile transition in porous rock: A review, *J. Struct. Geol.*, *44*, 25–53, doi:10.1016/j.jsg.2012.07.010.
- Wong, T., C. David, and W. Zhu (1997), The transition from brittle faulting to cataclastic flow in porous sandstones: Mechanical deformation, *J. Geophys. Res.*, *102*(B2), 3009–3025, doi:10.1029/96JB03281.
- Wong, T., P. Baud, and E. Klein (2001), Localized failure modes in a compactant porous rock, *Geophys. Res. Lett.*, *28*(13), 2521–2524, doi:10.1029/2001GL012960.
- Yin, H., J. Zhang, L. Meng, Y. Liu, and S. Xu (2009), Discrete element modeling of the faulting in the sedimentary cover above an active salt diapir, *J. Struct. Geol.*, *31*(9), 989–995, doi:10.1016/j.jsg.2008.10.007.
- Zhang, J., T. Wong, and D. Davis (1990), Micromechanics of pressure-induced grain crushing in porous rocks, *J. Geophys. Res.*, *95*(B1), 341–352, doi:10.1029/JB095iB01p00341.